ORIGINAL ARTICLE

Estimation for iron contamination in Si solar cell by ideality factor: deep neural network approach

Oleg Olikh[1] | **Oleg Lozitsky**[1] | **Oleksii Zavhorodnii**[1]

[1]Taras Shevchenko National University of Kyiv, 64/13, Volodymyrska Street, Kyiv, 01601, Ukraine

Correspondence
Olikh O, Taras Shevchenko National University of Kyiv, 64/13, Volodymyrska Street, Kyiv, 01601, Ukraine
Email: olegolikh@knu.ua

Funding information
National Research Foundation of Ukraine, Project Number: 2020.02/0036

Defect-assisted recombination often restricts the performance of photovoltaic devices and in order to mass-produce reliable solar cells low cost express methods are in demand which could monitor contamination during the process of manufacture. In our work, we applied the deep learning-based approach for estimating iron concentration in silicon solar cells by using ideality factor. The simulation of solar cells with the back surface field design for generating labeled training and test datasets was performed using SCAPS-1D software. Our results demonstrate that deep neural networks can predict iron concentration using the ideality factor, temperature, base-thickness and doping level of solar cells. Our simulation showed smaller prediction errors at high doping level, low temperature, and the two values of ideality factor: the first one for structures containing only iron interstitial atoms and the second for structures where Fe_i and iron-boron pairs coexist. The proposed method was tested on real silicon structures.

KEYWORDS
ideality factor, silicon, n^+–p–p^+ structure, iron contamination, SCAPS, machine learning

1 | INTRODUCTION

Metal contamination control remains an important challenge for silicon processing in microelectronics, logic technologies and manufacture of solar cells (SCs) [1, 2, 3, 4]. Typically, metal related defects are characterised by Fourier-transform infrared spectroscopy, electron-paramagnetic resonance, minority carrier lifetime measurements, deep level transient spectroscopy (DLTS), Laplace DLTS, etc [5, 6, 7]. However, these techniques are time-consuming, require special equipment or/and specially prepared samples. At the same time, the rapid standard SC characterization technique widely used in industry today is current-voltage (IV) measurements. IV characteristics contain important information about electrically active defects [6, 8]. Researchers propose several methods based on IV characteristics to diagnose the defects [6, 8, 9, 10, 11] and consider temperature dependencies of current components [10, 11] or IV differential parameters [8, 9]. These methods, however, require numerous IV measurements (in the first case) or IV measurements of high accuracy (in the second case).

In our previous work [12], we show that iron concentration (N_{Fe}) can be estimated by using SC ideality factor (n), which is used quite often to characterize semiconductor barrier structures of different types [13, 14, 15, 16, 17]. However, the defect signatures are convoluted in the ideality factor with the signatures from many other physical processes. As a result, the analytically obtained expressions for $N_{Fe} = f(n)$ are not universal and numerous grading curves have to be used to determine N_{Fe}; moreover, IV must be measured in a range of temperatures [12].

Over the last decade, various fields of theoretical and applied physics have successfully been solving different problems which do not involve rigid algorithmization by using deep learning methods [18, 19, 20]. Moreover, the authors claim [21] that materials informatics (combination of material property calculations/measurements and algorithms of informatics) has become the fourth (along with theory, simulations and experiments) paradigm of science. In our work too we apply deep learning for predicting iron concentration from the ideality factor (so to say "deep learning for deep levels"). Unlike in [12], we applied it to n^+–p–p^+ structure with back surface field (BSF) and took into account the influence of the base thickness on the ideality factor.

In our work, we consider a rather simple system that consists of crystalline silicon (c-Si) SC and iron impurity. Despite its simplicity, the system is important for practical applications since silicon solar cells constitute 90% of current global production capacity [22] and BSF is one of the popular designs that have been used in mass-production of c-Si SCs up to now [23, 24]. Surely, the passivated emitter and rear cell technology has recently come to the fore, but PERC solar cells also contain n^+–p junction and local n^+–p–p^+ junction [24, 25]. Iron in these structures is the main and one of the most detrimental metallic impurities [2, 3, 4]. The flowchart of the heuristic approach we used is shown in Fig. 1 where the following steps can be distinguished. First, the dark IV characteristics were simulated for SCs with varied parameters and known contaminant composition. In our numerical simulation, we applied SCAPS-1D [26, 27] widely used to model solar cells [28, 29, 30, 31, 32, 33]. Second, the obtained IV curves were fitted according to the double-diode model and the ideality factors were estimated. In the result, the labeled datasets were produced. Obviously, the labeled dataset from experimental IVs would be preferable, but in practice it is almost impossible to find thousands of samples with the required parameters. Third, the deep neural network (DNN) was trained to estimate iron contamination by using SC's base thickness, doping level, temperature and the ideality factor. Fourth, the DNN was tested by using both synthetic and experimental IV curves.

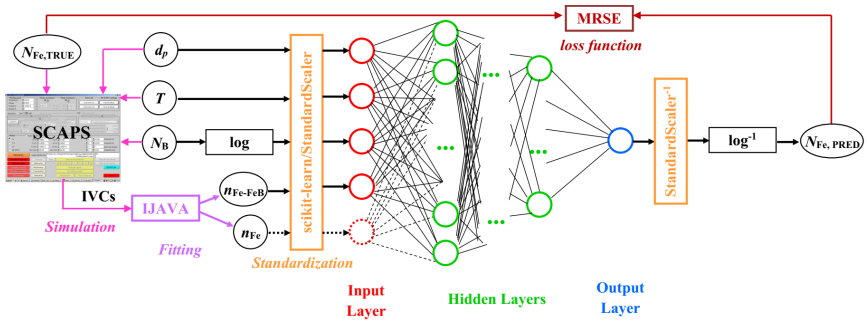

FIGURE 1 Scheme of deep learning-based approach for predicting iron concentration. Additional details are discussed in the body of the article.

2 | SIMULATION DETAILS

The n^+–p–p^+ structure used in calculations had 0.5 μm thick emitter layer n^+ with donor concentration $N_D = 10^{19}$ cm^{-3}; the p-layer and p^+-layer were uniformly doped with boron; the base p had the thickness $d_p = 150$–240 μm and dopant concentration $N_B = 10^{15}$–10^{17} cm^{-3}; the BSF-layer p^+ had the thickness d_{BSF} (1 μm) and the acceptor concentration $N_{BSF} = 5 \times 10^{18}$ cm^{-3}.

The simulations were carried out over the temperature range 290 – 340 K. For each temperature, the SCAPS setting file was created by using the following material parameters. The bandgap E_G and bandgap narrowing ΔE_G models were taken from Pässler [34] and Yan and Cuevas [35] respectively:

$$E_G = E_{G0} - \alpha\Theta\left\{\frac{1-3\Delta^2}{e^{\frac{\Theta}{T}}-1} + \frac{3\Delta^2}{2}\left(\sqrt[6]{1+\frac{\pi^2}{3(1+\Delta^2)}\left(\frac{2T}{\Theta}\right)^2 + \frac{3\Delta^2-1}{4}\left(\frac{2T}{\Theta}\right)^3 + \frac{8}{3}\left(\frac{2T}{\Theta}\right)^4 + \left(\frac{2T}{\Theta}\right)^6} - 1\right)\right\}, \quad (1)$$

$$\Delta E_G = 4.20 \times 10^{-5}\left[\ln\left(\frac{N_D}{10^{14}}\right)\right]^3; \qquad \Delta E_G = 4.72 \times 10^{-5}\left[\ln\left(\frac{N_{B,BSF}}{10^{14}}\right)\right]^3, \quad (2)$$

where $E_{G0} = 1.1701$ eV, $\alpha = 3.23 \times 10^{-4}$ eV/K, $\Theta = 446$ K, $\Delta = 0.51$. The carrier thermal velocities were calculated from the model suggested by Green [36]:

$$\upsilon_{th,n} = \sqrt{\frac{8qkT}{0.28 m_0 \pi}}; \qquad \upsilon_{th,p} = \sqrt{\frac{8qkT}{0.41 m_0 \pi}}, \quad (3)$$

where m_0 is a free electron mass. The effective state density masses in the conduction band m^*_{dC} and valence band m^*_{dV} were calculated according to the model from Couderc et al. [37]

$$\left(\frac{m^*_{dC}}{m_0}\right)^{1.5} = 1.094 - 1.312 \times 10^{-5}T + 6.753 \times 10^{-7}T^2 + 4.609 \times 10^{-10}T^3, \quad (4)$$

$$\left(\frac{m^*_{dV}}{m_0}\right)^{1.5} = 0.3426 + 3.376 \times 10^{-3}T - 4.689 \times 10^{-6}T^2 + 2.525 \times 10^{-9}T^3. \quad (5)$$

The carrier mobilities and the free carrier effective masses were taken from Klaassen [38] and O'Mara et al. [39], respectively. The temperature and doping dependencies of Auger recombination coefficients were calculated from

models by Altermatt et al. [40]:

$$C_p(T) = (7.91\times10^{-32} - 4.13\times10^{-35}T + 3.59\times10^{-37}T^2) \times\left(1+\left(564812T^{-1.6545}-1\right)\left(1-\tanh\left[\left\{\frac{p}{5\times10^{16}}\right\}^{0.29}\right]\right)\right), \quad (6)$$

$$C_n(T) = 2.8\times10^{-31}\times\left(1+\left(235548T^{-1.5013}-1\right)\left(1-\tanh\left[\left\{\frac{n}{5\times10^{16}}\right\}^{0.34}\right]\right)\right). \quad (7)$$

The band-to-band radiation recombination coefficient was taken from Nguyen et al. [41].

The outside surface recombination with electron and hole velocities 10^3 cm/s ware taken into account. For metal contacts on the rear and front surfaces, the flat bands' conditions were assumed.

The simulations were carried out under the assumption that defect–assisted recombination corresponds only to iron–related deep levels. As the base and SBF-layer are uniform contaminants, iron is assumed to be in concentration $N_{\mathrm{Fe}} = 10^{10}$–$10^{13}$ cm^{-3}. It is known that Fe in silicon can be in two states: in the form of FeB pair or in the interstitial state Fe_i. At near room temperature and boron concentration $> 10^{14}$ cm^{-3}, almost all Fe bound in FeB pairs is in equilibrium [42, 43, 44, 45]. According to Wijaranakula[42], the concentration of interstitial iron atoms N_{Fe_i} which remain unpaired in equilibrium state depend on temperature, doping level, and Fermi level F position. The estimations show that at 340 K $N_{\mathrm{Fe}_i} \simeq 0.1 N_{\mathrm{Fe}}$ for $N_{\mathrm{B}} \simeq 10^{15}$ cm^{-3} in the quasi-neutral region of SC base. However, numerous researches show that temporarily dissociation of pairs can be performed either by heating to the temperature above 200°C, or by applying intense illumination at room temperature [43, 45].

The simulations were performed for the following two cases. In the first case, the concentration of totally dissolved iron was given by a sum of concentrations of interstitial iron atoms Fe_i and trigonal iron-boron pairs $\mathrm{Fe}_i\mathrm{B}_s$:

$$N_{\mathrm{Fe}} = N_{\mathrm{Fe}_i} + N_{\mathrm{Fe}_i\mathrm{B}_s}\,. \quad (8)$$

The defect distributions in base and p^+-layer are inhomogeneous, depend on the Fermi level F position, and are given by [46, 42]:

$$\frac{N_{\mathrm{FeB}}}{N_{\mathrm{Fe}}} = \frac{N_{\mathrm{B}}10^{-23}\exp\left(-\frac{E_b}{kT}\right)}{\left[1+\frac{N_{\mathrm{B}}}{10^{23}}\exp\left(-\frac{E_b}{kT}\right)\right]\left[1+\exp\left(-\frac{F-E_{\mathrm{Fe}_i}}{kT}\right)\right]}, \quad N_{\mathrm{Fe}_i} = N_{\mathrm{Fe}} - N_{\mathrm{FeB}}\,, \quad (9)$$

where $E_b = 0.582$ eV is the binding energy of $\mathrm{Fe}_i\mathrm{B}_s$ pairs, E_{Fe_i} is the donor level associated with Fe_i. This case corresponds to the equilibrium condition and in this article it will be referred to as "Fe-FeB".

In the second case, Fe_i was assumed to be homogeneously distributed ($N_{\mathrm{Fe}_i} = N_{\mathrm{Fe}}$). This condition can be realized by heat treatment (210°C, 3 min) [47] or intense illumination [48]. This case will be referred to as "Fe".

The donor level $E_{\mathrm{Fe}_i} = E_V + 0.394$ eV with electron $\sigma_{n,\mathrm{Fe}} = 3.47\times10^{-11}T^{-1.48}$ cm^2 and hole $\sigma_{p,\mathrm{Fe}} = 4.54\times10^{-16}\exp\left(-\frac{0.05}{kT}\right)$ cm^2 capture cross-sections [46, 49] was associated with Fe_i in our simulations. For $\mathrm{Fe}_i\mathrm{B}_s$ the donor level $E^{\mathrm{D}}_{\mathrm{FeB}} = E_V + 0.10$ eV, $\sigma^{\mathrm{D}}_{n,\mathrm{FeB}} = 4\times10^{-13}$ cm^2, $\sigma^{\mathrm{D}}_{p,\mathrm{FeB}} = 2\times10^{-14}$ cm^2 and acceptor level $E^{\mathrm{A}}_{\mathrm{FeB}} = E_C - 0.26$ eV, $\sigma^{\mathrm{A}}_{n,\mathrm{FeB}} = 5.1\times10^{-9}T^{-2.5}$ cm^2, $\sigma^{\mathrm{A}}_{p,\mathrm{FeB}} = 3.32\times10^{-10}\exp\left(-\frac{0.262}{kT}\right)$ cm^2 [50, 46, 49] were used.

The dark forward IV characteristics were generated by SCAPS over a voltage range to 0.45 V. According to the

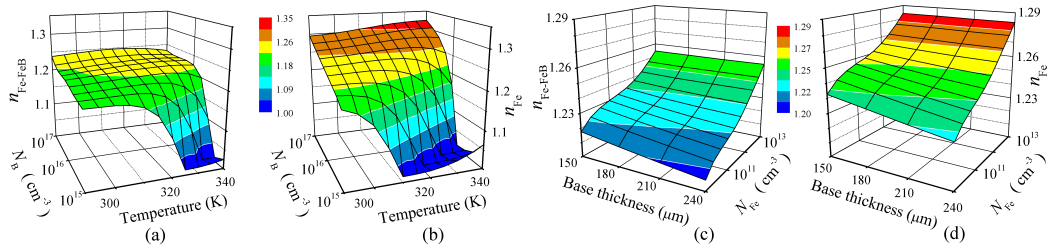

FIGURE 2 Ideality factor versus temperature and boron concentration (a, b) or base thickness and iron concentration (c,d). The Fe-FeB-case (a, c) and Fe-case (b, d). $N_{Fe} = 10^{10}$ cm^{-3} (a,b), $d_p = 180$ μm (a, b), $N_B = 10^{16}$ cm^{-3} (c, d), $T = 320$ K (c, d).

two-diode model, the dark SC current is given by [51]

$$I = I_{01}\left[\exp\left(-\frac{q(V - R_s I)}{kT}\right) - 1\right] + I_{02}\left[\exp\left(-\frac{q(V - R_s I)}{nkT}\right) - 1\right] + \frac{V - R_s I}{R_{sh}}, \tag{10}$$

where I_{01} and I_{02} are saturation currents, R_{sh} and R_s are shunt and series resistances. The two-diode model is often applied to describe real Si SCs: in Eq. (10) the first diode represents the "ideal" diode and the first term in the equation describes recombination in the base depth and emitter, including their surfaces; the second diode is the so-called recombination diode and the second term describes recombination within the depletion region [51]. The simulated data were fitted by Eq. (10) with n, I_{01}, I_{02}, R_{sh}, and R_s as fitting parameters. The fitting was performed by meta–heuristic method IJAVA [52]. The typical example of IV curves and fitting results is shown in Supplementary Material. It should be noted that i) the influence of both R_s (obtained values $< 10^{-2}$ Ω) and R_{sh} (obtained values $> 10^{18}$ Ω) can be neglected in the simulated IVs; ii) the contribution of recombination diode current is essential at low bias only and the voltage range $(0 - 0.45)$ V is quite sufficient to determine the ideality factor values accurately.

In our further calculations we used the ideality factors obtained in Fe-case and Fe-FeB-case which are referred to as n_{Fe} and n_{Fe-FeB} hereafter. The typical simulated dependencies of the ideality factor are shown in Fig. 2 and in Supplementary Material. The detailed discussion about n_{Fe} and n_{Fe-FeB} values are presented elsewhere [53], however it should be noted that (i) n can be the same for different values of SC parameters; (ii) dependencies of n_{Fe} and n_{Fe-FeB} differ not only in absolute values but also in behavior, although insignificantly.

3 | DEEP NEURAL NETWORK MODELS

Deep neural network training requires a large number of samples. In order to build a training dataset, we used IV characteristics simulated by using 4 d_p values, 9 N_B values, 11 T values, and 19 N_{Fe} values which are regularly distributed (for T and d_p in linear scale, for N_{Fe} and N_B in logarithmic scale) over the ranges 150–240 μm, 10^{15}–10^{17} cm^{-3}, 290 – 340 K, and 10^{10}–10^{13} cm^{-3}, respectively. Therefore, 7524 IV characteristics were simulated in Fe-case and in Fe-FeB-case.

In addition, several test datasets were prepared. For instance, the test dataset labeled "Fe-varied" consists of two subsets. The N_{Fe} values 1.300×10^{10}, 2.471×10^{10}, 4.696×10^{10}, 8.927×10^{10}, 1.697×10^{11}, 3.225×10^{11}, 6.130×10^{11}, 1.165×10^{120}, 2.214×10^{12}, 4.209×10^{12}, 8.000×10^{12} cm^{-3} (not used during training dataset creation), T values 290, 295, 300, 305, 310, 315, 320, 325, 330, 335, 340 K (used during training dataset creation), d_p value 180 μm (used

during training dataset creation), and N_B values 1.778×10^{15}, 5.623×10^{15}, 10^{16}, 3.162×10^{16}, 10^{17} cm^{-3} (used during training dataset creation) were used to prepare the first subset. Thus, the first subset is based on 605 pairs of IV characteristics. The N_{Fe} values 1.200×10^{110}, 2.234×10^{11}, 4.160×10^{11}, 7.746×10^{11}, 1.442×10^{12}, 2.685×10^{12}, 5.000×10^{12} cm^{-3} (not used during training dataset creation), T values 290, 300, 310, 320, 330, 340 K (used during training dataset creation), d_p values 210, 240 μm (used during training dataset creation), and N_B values 3.162×10^{15}, 10^{16}, 10^{17} cm^{-3} (used during training datset creation) were used to prepare the second subset of Fe-varied test dataset. Thus, Fe-varied test dataset is based on $605 + 252 = 857$ pairs of IV characteristics.

The similar approach was used to prepare "d-varied" (1189 samples), "T-varied" (832 samples), and "B-varied" (514 samples) test datasets. The base thickness, doping level, temperature, and iron concentration values which are different from those in training dataset values were used to prepare "All-varied" dataset (684 samples).

The precise values of parameters are listed in Supplementary Material.

We have tried to construct a DNN that could estimate iron contamination by using SC parameters (d_p and N_B), measured temperatures, and the result of IV fitting (the ideality factor). As shown in Fig. 1, two DNNs with different input parameters are under consideration. The input sample of the first DNN consists of $\{d_p, \log N_B, T, n_{Fe-FeB}\}$. In practice, this input set can be obtained from one dark IV measurement. This neural network is referred to as DNN_{FeFeB} hereafter. The second DNN uses $\{d_p, \log N_B, T, n_{Fe-FeB}, n_{Fe}\}$ in the input layer. In practice, to obtain a set like this additional SC processing (e.g., intense illumination) and two IV measurements are required. Further on this neural network is referred to as $DNN_{FeFeB-Fe}$.

The dense deep neural network was implemented through a high-level Keras API provided by TensorFlow [54]. The input layers consist of four or five nodes — see Fig. 1. In the output layer, one node and linear activation were used. The five configurations of the hidden layers were considered: (i) "pipe": each hidden layer contains equal number of nodes; (ii) "trapezium": six hidden layers, number of neurons linearly decreases from 100% (first layer) to 50% (last layer); (iii) "triangle": ten layers, number of neurons linearly decreases from 100% (first layer) to 10% (last layer); (iv) "butterfly": two serial reflected trapezium configurations; (v) "fir": two serial trapezium configurations.

The mean squared relative error (MSRE) was chosen as the loss function:

$$\mathrm{MSRE} = \frac{1}{N_s} \sum_{i=1}^{N_s} \frac{(N_{\mathrm{Fe,TRUE,i}} - N_{\mathrm{Fe,PRED,i}})^2}{N_{\mathrm{Fe,TRUE,i}} \cdot N_{\mathrm{Fe,PRED,i}}}, \tag{11}$$

where N_s is the number of samples in dataset, $N_{Fe,TRUE,i}$ is the iron concentration used in the i–th sample simulation, and $N_{Fe,PRED,i}$ is the DNN prediction for the i–th sample.

Hyperparameters include the number of nodes for the first hidden layer, the number of hidden layers (in pipe configuration), the batch size, the activation function, the optimizer, the learning rate, the preprocessing method, the dropout rate, the regularization function, the regularization rate, and the weight initializer. The grid search (coarse tuning to limit one hyperparameter) and random search (fine tuning) were performed over the predefined hyperparameter space shown in Table 1 and the best hyperparameter combination was chosen.

To estimate DNN training, 10–fold cross–validation was used. The performance of the DNN models on test datasets was evaluated by using three metrics: MSRE, coefficient of determination R^2, and coefficient of correlation R. Finally, to increase the DNNs performance, a full dataset consisting of training dataset and all the test datasets was used for training of the models.

TABLE 1 Hyperparameter space for DNNs.

Hyperparameter	Values
# nodes for first hidden layer	30, 40, 50, 75, 100, 120, 150
# hidden layers	4, 5, 6, 8, 10, 15
batch size	8, 16, 32, 64, 128
activation function	ReLu, sigmoid, tanh, SELU, ELU
optimizer	SGD, RMSprop, Adam, Adadelta, Adagrad, Adamax, Nadam, Ftrl
learning rate	10^{-5}, 10^{-4}, 10^{-3}, 10^{-2}
# epochs	100, 300, 400, 600, 1000, 1500
preprocessing method	StandartScaler, MinMaxScaler
regularization function	None, L2, L1, Dropout
regularization rate	10^{-5}, 10^{-4}, 10^{-3}, 10^{-2}
dropout rate	0.2, 0.3, 0.4, 0.5
weight initializer	Xavier Normal or Uniform, He Normal or Uniform, Random Normal or Uniform, Ones

4 | RESULTS AND DISCUSSION

4.1 | Synthetic IV curves

The results of hyperparameter search are listed in Table 2. In particular, for DNN_{FeFeB} and $DNN_{FeFeB-Fe}$ the trapezium and pipe configurations are chosen, respectively.

The training and test results of DNN_{FeFeB} are presented in Table 3, Table 4, and Fig. 3. As seen, MSRE of prediction by DNN_{FeFeB} is sufficiently large. However, it should be noted that in most cases the predictions with big differences between $N_{Fe,TRUE,i}$ and $N_{Fe,PRED,i}$ are not numerous. In particular, squared relative error (SRE) does not exceed 0.05 for 87%, 88%, and 96% samples in T-varied, d-varied and Fe-varid datasets respectively — see bars in Fig. 3. In the case of B-varied dataset (with doping level value non–used in the training dataset), the biggest MSRE = 1.06 is associated with those not often samples that have a really great SRE (>20) while SRE is less than 0.05 for 54% samples. The worst predictions are quite expectedly to be observed for the All-varied dataset: R^2 equals 0.813 and SRE<0.05 for only 18% samples. On the other hand, the Fe-varied dataset is most similar to real situation and the determination and correlation coefficients are high enough (0.991 and 0.996) in this case.

We have also considered the DNN prediction error versus SC parameters — see Figs. 4– 7. The figures present data for training dataset; the results for test datasets are similar (see Supplementary Material). In particular, Fig. 4(a) shows a considerable increase in prediction error, which is observed at $T > 320$ K for DNN_{FeFeB}. As seen from Fig. 4(c), at $T = 340$ K the maximum SRE is about 20 and SRE below 0.01 is observed for 55% of the samples whereas these values are equal to 0.02 and 83% at $T = 290$ K (Fig. 4(b)). It has been shown previously [53] that temperature rise causes the increase in the intrinsic recombination contributions to the ideality factor. As a result, the signature of Shockley-Read-Hall (SRH) recombination in n value becomes less prominent and DNN predictive ability decreases.

As shown in Fig. 5, the SC base thickness practically does not influence the prediction error (the mean value as well as relative frequency). However, as seen from Fig. 2(c,d), the ideality factor depends on base thickness at constant N_{Fe}. Therefore d_p is a significant parameter for DNN training

TABLE 2 Chosen hyperparameter combinations.

Hyperparameter	DNN_{FeFeB}	$DNN_{FeFeB-Fe}$
# nodes for hidden layers	120, 108, 96, 84, 72, 60	100, 100, 100, 100
batch size	32	32
activation function	ReLu	ELU
optimizer	Adamax	Adamax
learning rate	10^{-3}	10^{-3}
# epochs	400	1500
preprocessing method	StandartScaler	StandartScaler
regularization function	None	None
weight initializer	Xavier Normal	Xavier Normal

TABLE 3 Results of 10–fold cross–validation

Dataset	MSRE	
	DNN_{FeFeB}	$DNN_{FeFeB-Fe}$
training	0.31 ± 0.07	0.03 ± 0.01
full	0.28 ± 0.05	0.03 ± 0.01

TABLE 4 DNN's testing results

Dataset	DNN_{FeFeB}			$DNN_{FeFeB-Fe}$		
	MSRE	R^2	R	**MSRE**	R^2	R
T–varied	0.41	0.936	0.967	0.020	0.994	0.997
d–varied	0.37	0.961	0.980	0.018	0.996	0.998
B–varied	1.06	0.881	0.939	0.084	0.991	0.995
Fe–varied	0.06	0.991	0.996	0.005	0.999	0.999
All–varied	0.54	0.813	0.901	0.138	0.948	0.974

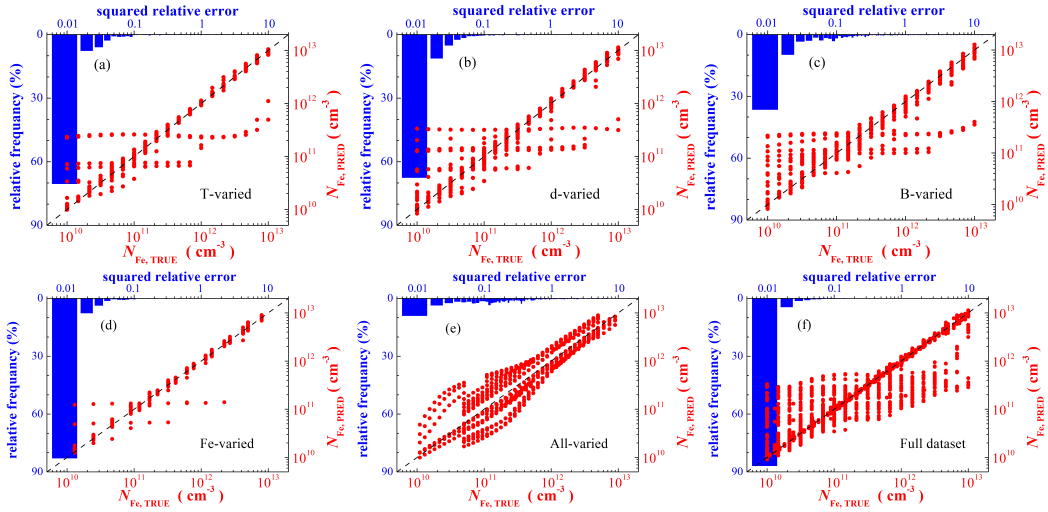

FIGURE 3 Iron concentrations are plotted against those generated by DNN_{FeFeB} on T-varied (a), d-varied (b), B-varied (c), Fe-varied (d), All-varied (e), and full (f) datasets (red points). Bars represent histograms of squared relative error. DNN was learned by training (a)–(e) or full (f) dataset. The black dashed lines are the identify lines servings as the references.

The predictive error increases sharply as the doping level decreases — see Fig. 6(a). In particular, the maximum SRE is about 0.05 for $N_B = 10^{17}$ cm^{-3} (Fig. 6(c)) whereas SRE below 0.05 is only for 56% of samples with $N_B = 10^{15}$ cm^{-3} (Fig. 6(b)). The occupation of holes in Fe-related level determines SRH recombination efficiency. According to the Fermi-Dirac statistics, the probability of hole occupation in a non-degenerate p-type semiconductor with full acceptor depletion can be expressed as

$$f_p = \frac{1}{1 + \frac{N_V}{N_B} \exp\left(\frac{E_V - E_{Fe_i}}{kT}\right)}. \tag{12}$$

If N_B decreases, the level is filled with the electron, the SRH recombination stops and the ideality factor value sharply decreases — Fig. 2(a,b). Moreover, in case of low doping, impurities have only a weak influence on the ideality factor, and therefore the increase of MSRE is observed. And finally, we believe that the additional factor causing the error to increase at high temperatures is the level filling.

Fig. 7(a) shows that MSRE increases at both low and high iron concentrations. The first N_{Fe} area of poor DNN accuracy is entirely predictable, the second one seems to be rather surprising. But according to Fig 7(c), the MSRE increase is most likely to be due to the fact that only a few samples are predicted with a great SRE at $N_{Fe} = 10^{13}$ cm^{-3} whereas SRE increases more systematically when $N_{Fe} = 10^{13}$ cm^{-3} — Fig 7(b).

The ideality factor value for the case when only interstitial iron (n_{Fe}) is available gives extra information about the defects in comparison with n_{Fe-FeB}. It is not surprising that $DNN_{FeFeB-Fe}$ has better operating parameters compared to DNN_{FeFeB} — see Table 3, Table 4, Fig. 8. The predictions improve: MSRE decreases, there is no huge difference between the values of $N_{Fe,TRUE}$ and $N_{Fe,PRED}$, the range of SRE becomes narrow (Figs. 4-8). As shown in Fig. 8, the maximum SRE does not exceed one even in the case of All-varied dataset, and SRE is below 0.02 for 93%, 92%, 73%, and 97% of the samples in T-varied, d-varied, B-varied, and Fe-varied datasets respectively. It should be noted that

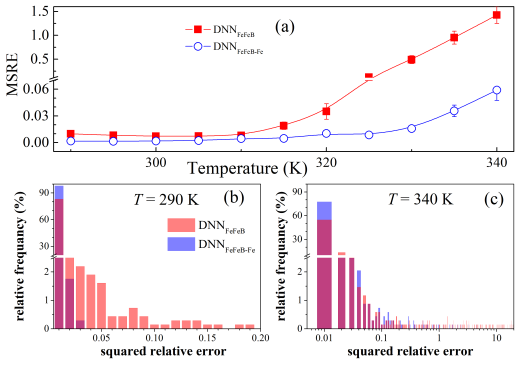

FIGURE 4 (a) Dependence of the MSRE (training dataset) on the temperature. (b),(c) Histograms of squared relative error for $T = 290$ K and $T = 340$ K. Red: $\mathrm{DNN_{FeFeB}}$; blue: $\mathrm{DNN_{FeFeB-Fe}}$.

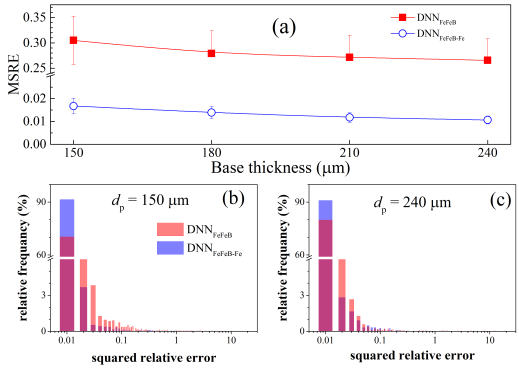

FIGURE 5 (a) Dependence of the MSRE (training dataset) on the base thickness. (b),(c) Histograms of squared relative error for $d_p = 150$ μm and $d_p = 240$ μm. Red: $\mathrm{DNN_{FeFeB}}$; blue: $\mathrm{DNN_{FeFeB-Fe}}$.

for Fe-varied datasets both R^2 and R are 0.999.

Despite the difference in prediction accuracy, the features of $\mathrm{DNN_{FeFeB-Fe}}$ and $\mathrm{DNN_{FeFeB}}$ are similar. Thus, the DNN training with N_B values, which are expected to be an object of future research, is important for the accuracy of prediction (Fig. 8); the increase in the temperature (Fig. 4) as well as decrease in doping level (Fig. 6) or iron concentration (Fig. 7) results in error increase. It should be noted that the prediction error gain with N_{Fe} increase is not observed in case of $\mathrm{DNN_{FeFeB-Fe}}$ and the range of SRE at $N_{Fe} = 10^{13}$ cm^{-3} is narrower than that at $N_{Fe} = 10^{10}$ cm^{-3} — see Fig. 7(b,c).

The results of both $\mathrm{DNN_{FeFeB}}$ and $\mathrm{DNN_{FeFeB-Fe}}$ training with a full dataset are presented in Table 3, Fig. 3(f), and Fig. 8(f). We can see that in our case the extension of the labeled dataset practically does not improve the result of DNN. In our opinion, this is an evidence of i) good DNN configuration tuning; ii) restricted predictive ability of $\mathrm{DNN_{FeFeB}}$, which is caused by ambiguity of dependence $n_{\mathrm{Fe-FeB}} = f(N_{\mathrm{Fe}})$.

4.2 | Experimental IV curves

The ability of DNNs to predict iron concentration in real silicon SCs was tested as well. The samples used in the experiment were n^+–p–p^+–Si structures. The structures were fabricated from p–type boron doped Czochralski silicon wafer with [100] orientation and resistivity of 10 Ohm·cm ($N_B = 1.4 \cdot 10^{15}$ cm^{-3}). The n^+ emitter with sheet resistance of about $(20 \div 30)$ Ω/□ and a thickness of 0.7 μm was formed by phosphorus diffusion at 940°; p^+ layer ($(10 \div 20)$ Ω/□, 0.6 μm) was formed by boron diffusion at 985°C. The base thickness was 350 μm. The area of the samples was 1.52×1.535 cm^2. The concentration of iron in the SC base $N_{\mathrm{Fe,MEAS}}$ was determined from kinetics of the short circuit current under monochromatic illumination [55]. Two samples used in the investigation are referred to as SC320 and SC349 with $N_{\mathrm{Fe,MEAS}}$ of $(2.0 \pm 0.4) \cdot 10^{12}$ cm^{-3} and $(6.7 \pm 0.7) \cdot 10^{12}$ cm^{-3}, respectively.

We can see that DNN was faced with a rather difficult task when the complexity was associated with a certain mismatch between the parameters of real structures and those used in the simulation. However, the need for iron-related defects, which predominantly determine recombination, was the main criterion for sampling in our case.

The dark IV characteristics of the samples were measured at temperatures 300, 320, and 340 K. The measure-

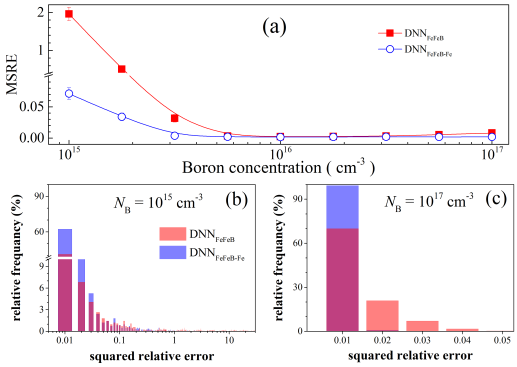

FIGURE 6 (a) Dependence of the MSRE (training dataset) on the boron concentration. (b),(c) Histograms of squared relative error for $N_B = 10^{15}$ cm^{-3} and $N_B = 10^{17}$ cm^{-3}. Red: DNN_{FeFeB}; blue: $DNN_{FeFeB-Fe}$.

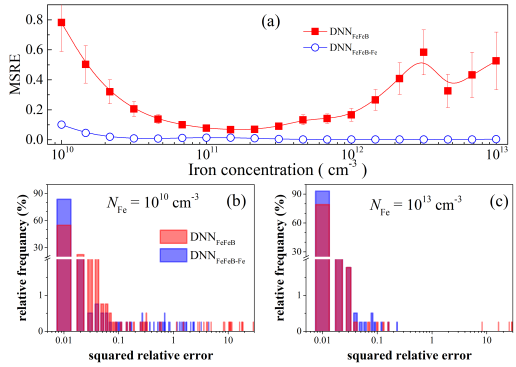

FIGURE 7 (a) Dependence of the MSRE (training dataset) on the iron concentration. (b),(c) Histograms of squared relative error for $N_{Fe} = 10^{10}$ cm^{-3} and $N_{Fe} = 10^{13}$ cm^{-3}. Red: DNN_{FeFeB}; blue: $DNN_{FeFeB-Fe}$.

TABLE 5 Results of experimental IV fitting and iron contamination testing

Sample	$N_{Fe,MEAS}$, 10^{12} cm^{-3}	T, K	n_{Fe-FeB}	$R_{sh,Fe-FeB}$, Ohm	n_{Fe}	$R_{sh,Fe}$, Ohm	$N_{Fe,PRED}$, 10^{12} cm^{-3}			
							DNN_{FeFeB}		$DNN_{FeFeB-Fe}$	
							training	full	training	full
SC320	2.0 ± 0.4	300	1.214	$1.6 \cdot 10^6$	1.195	$1.4 \cdot 10^6$	3.9	2.8	3.0	2.0
		320	1.204	$8.6 \cdot 10^5$	1.148	$8.0 \cdot 10^5$	6.6	1.9	16	19
		340	1.118	$4.3 \cdot 10^5$	1.111	$4.3 \cdot 10^5$	3.8	1.2	89	574
SC349	6.7 ± 0.7	300	1.223	$2.9 \cdot 10^6$	1.222	$2.6 \cdot 10^6$	8.9	5.6	15	11
		320	1.183	$1.7 \cdot 10^6$	1.182	$1.7 \cdot 10^6$	1.2	0.4	10	32
		340	1.138	$1.3 \cdot 10^6$	1.173	$1.3 \cdot 10^6$	9.8	1.7	26	411

ments were carried out after 48 h exposition in the dark at room temperature ("Fe-FeB" case) as well as immediately after intense illumination of the sample with a halogen lamp ("Fe" case). To fit the experimental data and determine fitting parameters, in particular n, R_s, R_{sh}, we used Eq. (10). The typical results of the measurements and approximations are shown in Fig. 9 and Table 5. It should be noted that for real IV curves, in contrast to synthetic ones, the influence of series and shunt resistances cannot be neglected (the magnitude of R_s is about 3 and 6 Ohm for samples SC320 and SC349, respectively, all the values of R_{sh} are listed in Table 5).

The ideality factors determined from the experimental curves and the sample parameters were used as input data for DNN_{FeFeB} and $DNN_{FeFeB-Fe}$, which were trained either on the training dataset or full dataset. The predictions are listed in Table 5.

First of all, it should be noted that even though we did not use a simulation model of extremely high complexity, the results exceeded our expectations. In particular, the predicted iron concentrations in DNN_{FeFeB} differed only several times from the measured ones. In the case of sample SC320 and DNN_{FeFeB} trained on the full dataset, the

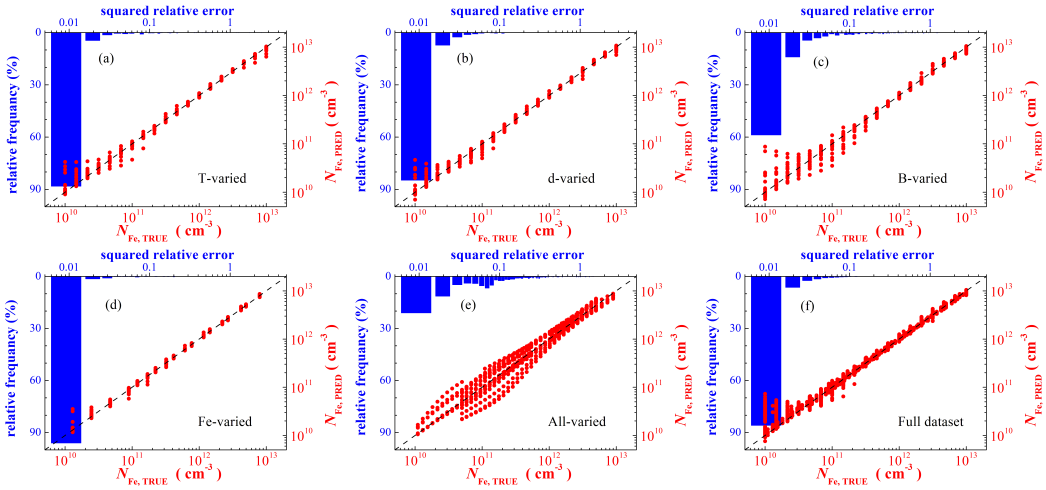

FIGURE 8 Iron concentrations are plotted against those generated by $DNN_{FeFeB-Fe}$ on T-varied (a), d-varied (b), B-varied (c), Fe-varied (d), All-varied (e), and full (f) datasets (red points). Bars represent histograms of squared relative error. DNN was learned by training (a)–(e) or full (f) dataset. The black dashed lines are the identify lines servings as the references.

error did not exceed 40%.

Also, it should be noted that the results confirm the trends revealed by the analysis of synthetic IV curves. In particular, the prediction accuracy decreases at $T > 320$ K and iron concentrations close to the upper limit in the range (10^{13} cm^{-3}). These facts completely coincide with the data in Fig. 4a and Fig. 7a, respectively. In addition, the sample's base doping level ($N_B = 1.4 \cdot 10^{15}$ cm^{-3}) is not used in the training dataset but can be found in the d–varied dataset (see Supplementary Material). Table 5 shows that the prediction of DNN_{FeFeB} trained by a full dataset is better than in the case of learning only by a training dataset, especially for SC320 sample. This fact confirms the conclusion made in the previous section about the importance of DNN training with N_B values, which are expected to be the object of future research.

On the other hand, contrary to our expectations, $DNN_{FeFeB-Fe}$ demonstrates worse performance than DNN_{FeFeB} in the majority case. The likely reasons are the following. First, the use of two ideality factor values makes the influence of simulation simplifications more significant (e.g., the effect of unaccounted processes that cause both shunt and series resistance). Secondly, to obtain a correct n_{Fe} is a more complicated experimental task than to determine n_{Fe-FeB}. For example, in our experiment it took about 100 s to obtain IV characteristics after intense illumination. This interval included the time required to set the temperature after illumination-induced heating and the time of measurement. According to [43, 56], the characteristic association time of FeB pairs at $T = 340$ K and $N_B = 1.4 \cdot 10^{15}$ cm^{-3} is about 600 s. That is, despite the potentially higher accuracy of the $DNN_{FeFeB-Fe}$ predictions (shown in the previous section), the practical application of this approach is more complicated.

On the whole, the results obtained for real SCs confirm the possibility to estimate iron contamination using the ideality factor.

Finally, we would like to suggest some speculations about the applicability of the trained DNNs to different SC structures. The speculations are based on assumption that the ideality factor distinguishes depletion-region recombination from most other sources of recombination [51, 57]. Certainly, there are some deviations from this rule for

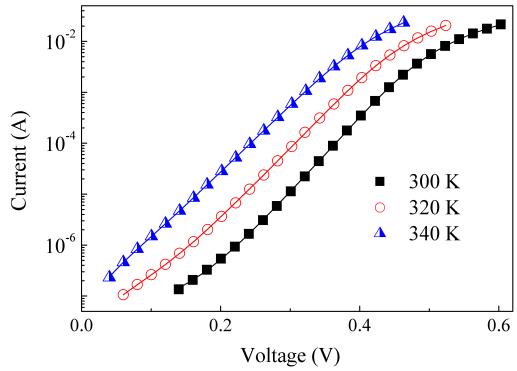

FIGURE 9 $I-V$ characteristics measured at 300 K, 320 K, and 340 K for sample SC320. The marks are the experimental results, and the solid lines are the curves fitted by Eq. (10).

real structures. For instance, our simulation reveals the n dependence on base thickness [53]. Nevertheless this dependence is weak, and the ideality factor value is mainly determined by depletion-region recombination.

First of all, the DNNs applicability depends on the requirement for Shockley–Read–Hall recombinationto be predominant. In case, if there are other mechanisms causing free carrier concentration to decrease, the models which diverge from the two-diode one are proposed (e.g., three-diode [58, 59]). Moreover, the base must be doped by boron. For example, if SC is prepared from Si:Al wafer, the simulation model which is used for training dataset preparation must be modified: the parameters of Fe_iAl_s pair as well as the changes in defect distribution (Eq. (9)) should be taken into consideration. Finally, if another type of defect (in addition to iron–related deep levels) is present in the solar cell, which also induces intensive SRH recombination, the simulation model must be more complicated as well. The primary competitors of Fe_iB_s are boron-oxygen complexes [60, 61] and oxide precipitates [62, 63] in Cz-Si. So the development of the corresponding model can be our next step. To the point, it should be noted that a high n value can serve an indicator of another defect presence: in our simulation this value is $n < 1.4$. The absence of non-iron active defects may be the most limiting factor of the DNNs applicability; in particular, this confined the selection of SCs for our experimental verification of the proposed method.

Thus, the trained DNNs can be applied to BSF solar cells prepared from Si:B wafers. It should be noted that the modern technique of crystal growth makes it possible to restrict oxygen concentration substantially even in solar grade Cz-Si. On the one hand, Al is used to produce the doped p^+ region at the industrial level [24, 25]. However, since a boron BSF is one of the promising techniques for achieving high quality back contact [64, 65] therefore the p^+ layer, which is doped by boron, was under our consideration. On the other hand, he probable p^+–layer influences this process mostly via the electric field. Therefore, the kind of doping atom in p^+–layer is not very important for simulation, and in our opinion, the DNNs is applicable for Al BSF cell as well. Besides, the recombination in the rear surface region is not crucially important for estimating the ideality factor. The wake aforesaid allows us to make a conclusion that the trained DNN can be applied to those PERC solar cell in which i) the base is boron-doped; ii) the iron-related deep levels are the main cause of defect-assisted recombination.

5 | CONCLUSION AND OUTLOOK

In this paper, we determined iron concentration in silicon BSF solar cells from the ideality factor value and systematically studied the performance of deep learning for the indicated task. It was the first attempt to use deep learning for retrieving deep level parameters from the current–voltage curve. In the model study, we performed simulation in order to obtain a training labeled dataset and test labeled datasets. In the end, DNN was trial-tested by using the parameters of actual solar cells. Our results showed the DNN ability to predict iron concentration by ideality factor, thickness and doping level of SC base as well as temperature. For synthetic datasets the MSRE was as small as 0.005. Our simulation shows the prospects for applying the ideality factor of two values (for structure with Fe_i only as well as with Fe_iB_s and Fe_i coexistence) in order to upgrade prediction accuracy. At the same time, the practical application of this approach demonstrated difficulties in obtaining correct data. It was important to train the DNN with boron concentration values, which agreed with the doping level of the structures under study. Moreover, the increase in iron or boron concentration, as well as temperature decrease, resulted in smaller prediction errors.

The proposed approach uses a simple and widely applied setup and does not take much time. Therefore, it could be easily integrated into the manufacturing environment. It should be noted, however, that for our purposes the task was simplified. Nevertheless, we believe that this DNN approach can be further improved in two ways. The first is to refine labeled datasets by using 3D-simulators (e.g., SILVACO TCAD) or real IV measurements in a broad set of SCs. The second is to improve DNN operation, and fine-tuning seems to be most promising in this case. For example, innumerous input parameters can be multiplied and transformed into a picture so that the vision model (e.g., VGG16) could be applied.

Acknowledgments

This work was supported by National Research Foundation of Ukraine (project number 2020.02/0036)

Conflict of Interest

The authors declare that they have no known competing financial interests or personal relationships that could have appeared to influence the work reported in this paper.

Data availability

The simulated IV characteristics, n_{Fe} and n_{Fe-FeB} values, and trained DNNs are available at *https://github.com/olegolikh/IVcharacteristics.git*.

References

[1] Claeys C, Simoen E. Metal Impurities in Silicon- and Germanium-Based Technologies: Origin, Characterization, Control, and Device Impact, vol. 270 of Springer Series in Materials Science. Berlin/New York: Springer International Publishing; 2018.

[2] Zhu H, Yu X, Zhu X, Wu Y, He J, Vanhellemont J, et al. Low temperature iron gettering by grown-in defects in p–type Czochralski silicon. Superlattices Microstruct 2016 Nov;99:192–196.

[3] Schmidt J. Effect of Dissociation of Iron–Boron Pairs in Crystalline Silicon on Solar Cell Properties. Progress in Photovoltaics: Research and Applications 2005 Jun;13(4):325–331.

[4] Schubert MC, Padilla M, Michl B, Mundt L, Giesecke J, Hohl-Ebinger J, et al. Iron related solar cell instability: Imaging analysis and impact on cell performance. Sol Energy Mater Sol Cells 2015 Jul;138:96–101.

[5] Schroder DK. Semiconductor Material and Device Characterization. Third ed. New Jersey: John Wiley & Sons; 2006.

[6] Kurchin RC, Poindexter JR, Vähänissi V, Savin H, del Cañizo C, Buonassisi T. How Much Physics is in a Current-Voltage Curve? Inferring Defect Properties From Photovoltaic Device Measurements. IEEE J Photovolt 2020 Nov;10(6):1532–1537.

[7] Peaker AR, Markevich VP, Coutinho J. Tutorial: Junction spectroscopy techniques and deep-level defects in semiconductors. J Appl Phys 2018;123(16):161559.

[8] Bulyarskiy SV, Lakalin AV, Saurov MA, Gusarov GG. The effect of vacancy-impurity complexes in silicon on the current-voltage characteristics of p-n junctions. J Appl Phys 2020 Oct;128(15):155702.

[9] Bulyarskiy SV. The effect of electron-phonon interaction on the formation of reverse currents of p-n-junctions of silicon-based power semiconductor devices. Solid-State Electron 2019 Oct;160:107624.

[10] Claeys C, Simoen E. Device Performance as a Metrology Tool to Detect Metals in Silicon. physica status solidi (a) 2019 Sep;216(17):1900126.

[11] Simoen E, Claeys C, Vanhellemont J. Defect Analysis in Semiconductor Materials Based on p-n Junction Diode Characteristics. In: Defects and Diffusion in Semiconductors - An Annual Retrospective IX, vol. 261 of Defect and Diffusion Forum Trans Tech Publications Ltd; 2007. p. 1–24.

[12] Olikh OY. Relationship between the ideality factor and the iron concentration in silicon solar cells. Superlattices Microstruct 2019 Dec;136:106309.

[13] van der Heide ASH, Schonecker A, Bultman JH, Sinke WC. Explanation of High Solar Cell Diode Factors by Nonuniform Contact Resistance. Progress in Photovoltaics: Research and Applications 2005 Jan;13(1):3–16.

[14] Duan L, Yi H, Xu C, Upama MB, Mahmud MA, Wang D, et al. Relationship Between the Diode Ideality Factor and the Carrier Recombination Resistance in Organic Solar Cells. IEEE Journal of Photovoltaics 2018 Nov;8(6):1701–1709.

[15] Chen J, Zhu M, Lu X, Zou X. Electrical characterization of GaN Schottky barrier diode at cryogenic temperatures. Appl Phys Lett 2020 Feb;116(6):062102.

[16] Dalapati P, Manik NB, Basu AN. Analysis of the Temperature Dependence of Diode Ideality Factor in InGaN-Based UV-A Light-Emitting Diode. Semiconductors 2020 Oct;54(10):1284–1289.

[17] Calado P, Burkitt D, Yao J, Troughton J, Watson TM, Carnie MJ, et al. Identifying Dominant Recombination Mechanisms in Perovskite Solar Cells by Measuring the Transient Ideality Factor. Phys Rev Applied 2019 Apr;11:044005.

[18] Carleo G, Cirac I, Cranmer K, Daudet L, Schuld M, Tishby N, et al. Machine learning and the physical sciences. Rev Mod Phys 2019 Dec;91:045002.

[19] Ju S, Shimizu S, Shiomi J. Designing thermal functional materials by coupling thermal transport calculations and machine learning. J Appl Phys 2020 Oct;128(16):161102.

[20] Rodrigues S, Ramos HG, Morgado-Dias F. Machine learning PV system performance analyser. Prog Photovoltaics Res Appl 2018 Aug;26(8):675–687.

[21] Ju S, Shimizu S, Shiomi J. Designing thermal functional materials by coupling thermal transport calculations and machine learning. J Appl Phys 2020 Oct;128(16):161102.

[22] Jean J, Brown PR, Jaffe RL, Buonassisi T, Bulović V. Pathways for solar photovoltaics. Energy Environ Sci 2015 Jul;8(4):1200–1219.

[23] Ajayan J, Nirmal D, Mohankumar P, Saravanan M, Jagadesh M, Arivazhagan L. A review of photovoltaic performance of organic/inorganic solar cells for future renewable and sustainable energy technologies. Superlattices Microstruct 2020 Jul;143:106549.

[24] Green MA. Photovoltaic technology and visions for the future. Prog Energy 2019 Jul;1(1):013001.

[25] Wilson GM, Al-Jassim M, Metzger WK, Glunz SW, Verlinden P, Xiong G, et al. The 2020 photovoltaic technologies roadmap. J Phys D: Appl Phys 2020 Sep;53(49):493001.

[26] Burgelman M, Nollet P, Degrave S. Modelling polycrystalline semiconductor solar cells. Thin Solid Films 2000 Feb;361–362:527–532.

[27] Decock K, Khelifi S, Burgelman M. Modelling multivalent defects in thin film solar cells. Thin Solid Films 2011 Aug;519(21):7481–7484.

[28] Hu ET, Yue GQ, Zhang RJ, Zheng YX, Chen LY, Wang SY. Numerical simulations of multilevel impurity photovoltaic effect in the sulfur doped crystalline silicon. Renewable Energy 2015 May;77:442–446.

[29] Hamache A, Sengouga N, Meftah A, Henini M. Modeling the effect of 1 MeV electron irradiation on the performance of n^+-p-p^+ silicon space solar cells. Radiat Phys Chem 2016 Jun;123:103–108.

[30] Kim K, Gwak J, Ahn SK, Eo YJ, Park JH, Cho JS, et al. Simulations of chalcopyrite/c-Si tandem cells using SCAPS-1D. Sol Energy 2017;145:52–58.

[31] Cappelletti MA, Casas GA, Cédola AP, y Blancá ELP, Soucase BM. Study of the reverse saturation current and series resistance of p-p-n perovskite solar cells using the single and double-diode models. Superlattices Microstruct 2018 Nov;123:338–348.

[32] Boubakeur M, Aissat A, Ben Arbia M, Maaref H, Vilcot JP. Enhancement of the efficiency of ultra-thin CIGS/Si structure for solar cell applications. Superlattices Microstruct 2020 Feb;138:106377.

[33] Casas GA, Cappelletti MA, Cédola AP, Soucase BM, Peltzer y Blancá EL. Analysis of the power conversion efficiency of perovskite solar cells with different materials as Hole-Transport Layer by numerical simulations. Superlattices Microstruct 2017;107:136–143.

[34] Pässler R. Dispersion-related description of temperature dependencies of band gaps in semiconductors. Phys Rev B 2002 Aug;66:085201.

[35] Yan D, Cuevas A. Empirical determination of the energy band gap narrowing in p^+ silicon heavily doped with boron. J Appl Phys 2014 Nov;116(19):194505.

[36] Green MA. Intrinsic concentration, effective densities of states, and effective mass in silicon. J Appl Phys 1990 Mar;67(6):2944–2954.

[37] Couderc R, Amara M, Lemiti M. Reassessment of the intrinsic carrier density temperature dependence in crystalline silicon. J Appl Phys 2014 Mar;115(9):093705.

[38] Klaassen DBM. A unified mobility model for device simulation — I. Model equations and concentration dependence. Solid-State Electron 1992 Jul;35(7):953– 959.

[39] O'Mara WC, Herring RB, Hant LP. Handbook of semiconductor silicon technology. New Jersey, USA: Noyes Publications; 1990.

[40] Altermatt PP, Schmidt J, Heiser G, Aberle AG. Assessment and parameterisation of Coulomb–enhanced Auger recombination coefficients in lowly injected crystalline silicon. J Appl Phys 1997 Nov;82(10):4938–4944.

[41] Nguyen HT, Baker-Finch SC, Macdonald D. Temperature dependence of the radiative recombination coefficient in crystalline silicon from spectral photoluminescence. Appl Phys Lett 2014 Mar;104(11):112105.

[42] Wijaranakula W. The Reaction Kinetics of Iron–Boron Pair Formation and Dissociation in P–Type Silicon. J Electrochem Soc 1993 Jan;140(1):275–281.

[43] Möller C, Bartel T, Gibaja F, Lauer K. Iron-boron pairing kinetics in illuminated p-type and in boron/phosphorus co-doped n-type silicon. J Appl Phys 2014 Jul;116(2):024503.

[44] Tan J, Macdonald D, Rougieux F, Cuevas A. Accurate measurement of the formation rate of iron–boron pairs in silicon. Semicond Sci Technol 2011 Mar;26(5):055019.

[45] Macdonald D, Roth T, Deenapanray PNK, Bothe K, Pohl P, Schmidt J. Formation rates of iron-acceptor pairs in crystalline silicon. J Appl Phys 2005 Oct;98(8):083509.

[46] Murphy JD, Bothe K, Olmo M, Voronkov VV, Falster RJ. The effect of oxide precipitates on minority carrier lifetime in p–type silicon. J Appl Phys 2011 Sep;110(5):053713.

[47] Zoth G, Bergholz W. A fast, preperetion-free method to detect iron in silicon. J Appl Phys 1990 Jun;67(11):6764–6771.

[48] Geerligs LJ, Macdonald D. Dynamics of light-induced FeB pair dissociation in crystalline silicon. Appl Phys Lett 2004 Nov;85(22):5227–5229.

[49] Rougieux FE, Sun C, Macdonald D. Determining the charge states and capture mechanisms of defects in silicon through accurate recombination analyses: A review. Sol Energy Mater Sol Cells 2018 Dec;187:263 – 272.

[50] Istratov AA, Hieslmair H, Weber ER. Iron and its complexes in silicon. Applied Physics A: Materials Science & Processing 1999 Jul;69(1):13–44.

[51] Breitenstein O. Understanding the current-voltage characteristics of industrial crystalline silicon solar cells by considering inhomogeneous current distributions. Opto–Electronics Review 2013 Sep;21(3):259–282.

[52] Yu K, Liang JJ, Qu BY, Chen X, Wang H. Parameters identification of photovoltaic models using an improved JAYA optimization algorithm. Energy Conversion and Management 2017 Oct;150:742–753.

[53] Olikh OY, Zavhorodnii OV. Modeling of ideality factor value in n^+–p–p^+–Si structure. Journal of Physical Studies 2020;24(4):4701.

[54] Chollet F. Deep Learning with Python. Second ed. Manning; 2017.

[55] Olikh O, Kostylyov V, Vlasiuk V, Korkishko R. Estimation of Iron Concenration in Silicon Solar Cell by Kinetics of Light-Induced Change in Short-Circuit Current. In: II International Advanced Study Conference Condensed Matter and Low Temperature Physics CM&LTP 2021. Book of Abstracts. Kharkiv, Ukraine. Kharkiv; 2021. p. 191.

[56] Khelifati N, Laine HS, Vähänissi V, Savin H, Bouamama FZ, Bouhafs D. Dissociation and Formation Kinetics of Iron–Boron Pairs in Silicon after Phosphorus Implantation Gettering. Phys Status Solidi A 2019 Sep;216(17):1900253.

[57] McIntosh K, Altermatt P, Heiser G. Depletion–region recombination in silicon solar cells. When does $mDR = 2$? In: 16th European Photovoltaic Solar Energy Conference: Proceedings of the International Conference and Exhibition Publisher:James and James (Science Publishers) Ltd; 2000. p. 250–253.

[58] Hallam BJ, Hamer PG, Bonilla RS, Wenham SR, Wilshaw PR. Method of Extracting Solar Cell Parameters From Derivatives of Dark I–V Curves. IEEE Journal of Photovoltaics 2017 Sep;7(5):1304–1312.

[59] Shah JM, Li YL, Gessmann T, Schubert EF. Experimental analysis and theoretical model for anomalously high ideality factors ($n \gg 2.0$) in AlGaN/GaN p–n junction diodes. J Appl Phys 2003 Aug;94(4):2627–2630.

[60] Lindroos J, Savin H. Review of light-induced degradation in crystalline silicon solar cells. Sol Energy Mater Sol Cells 2016 Apr;147:115–126.

[61] Niewelt T, Schöon J, Warta W, Glunz SW, Schubert MC. Degradation of Crystalline Silicon Due to Boron–Oxygen Defects. IEEE Journal of Photovoltaics 2017 Jan;7(1):383 –398.

[62] Murphy JD, McGuire JD, Bothe K, Voronkov VV, Falster RJ. Minority carrier lifetime in silicon photovoltaics: The effect of oxygen precipitation. Sol Energy Mater Sol Cells 2014 Jan;120:402–411.

[63] Chen L, Yu X, Chen P, Wang P, Gu X, Lu J, et al. Effect of oxygen precipitation on the performance of Czochralski silicon solar cells. Sol Energy Mater Sol Cells 2011 Nov;95(11):3148–3151.

[64] Kim DS, Nakayashiki K, Rounsaville B, Meemongkolkat V, Rohatgi A. Silicon solar cells with boron back surface field formed by using boric acid. In: 22th European Photovoltaic Solar Energy Conference: Proceedings of the International Conference and Exhibition; 2007. p. 1730–1733.

[65] Du G, Chen B, Chen N, Hu R. Efficient Boron Doping in the Back Surface Field of Crystalline Silicon Solar Cells via Alloyed-Aluminum–Boron Paste. IEEE Electron Device Letters 2012;33(4):573–575.